Journal of Sound and Vibration (1998) **212**(2), 215–230

DYNAMIC STABILITY OF ROTATING COMPOSITE SHAFTS UNDER PERIODIC AXIAL COMPRESSIVE LOADS

L.-W Chen and W.-K. Peng

Department of Mechanical Engineering, *National Cheng Kung University*, *Tainan*, *Taiwan* 70101, *Republic of China*

(*Received* 18 *December* 1996, *and in final form* 31 *July* 1997)

This paper describes the dynamic behavior of a rotating composite shaft subjected to axial periodic forces using the finite element method. Laminated composite shafts are modelled using Timoshenko beams. The numerical results show good agreement with the reported beams models. Effects of static and time dependent components of axial loads on the stability of the composite shaft are studied. This paper also investigates the effect of the rotational speeds and the disk on the unstable regions of the shaft. The numerical results show that for the same geometric parameters, a steel shaft has a lower frequency than that of the composite shafts; however, the steel shaft is more stable than composite shafts because the shaft–disk system is subjected to axial periodic forces at lower rotational speeds. Also, the effect of the gyroscopic moments makes the steel shaft more sensitive to the periodic axial load than the composite one.

1. INTRODUCTION

Sturdy and robust fiber-reinforced composite materials, with high strength and stiffness ratios coupled with a low specific weight, are attractive for developing light weight drive shafts. The designed composite shafts are often in the form of multilaminar cylindrical shells. Therefore, shell theory can be used to study the vibration characteristics of the composite shafts. Most studies for the analysis of shells are based on either the classical shell theory or thick shell theories. Classical shell theory is widely used for analyzing thin shells, although it is simple and neglects the transverse shear effects. Thin shell analyses of composite material have been performed by Dong [1] using Donnell's shallow shell theory, by Bert *et al*. [2] using Love's first approximation theory and by Padovan [3] using Novozhilov's higher order theory. Thick shells are analyzed, including the shear deformation effect, and the Donnell's, Love's and Sanders' theories were developed [4–7]. Bert and Kumar [8] presented a model for moderately thick shells by considering thickness shear deformation and rotatory inertia for predicting the free vibrational behavior of complete cylindrical shells cross-ply laminated bimodulus composite materials. Rotating shells were studied by Fox and Harkie [9] using Flügge's thin shell theory, by Smirnov [10] using Novozhilov's shell theory, and by Chen *et al*. [11] to describe the vibrations at high rotating speeds undergoing large deformations. The frequencies and damping factor of rotating cylindrical shells were studied by Sivadas and Ganesan [12], who used theory for moderately thick shells and considered shear deformation and rotatory inertia.

0022–460X/98/170215 + 16 $25.00/0/sv971405

Zinberg and Symonds [13] analyzed the vibration of composite shafts to investigate the critical speeds for rotating anisotropic shafts; their experiments confirmed the advantages of composite shafts over aluminum alloy shafts. Reis *et al*. [14] used Donnell's thin shell theory and applied finite element method to evaluate critical speeds of thin-walled laminated composite shafts, and concluded that the lay-up of a composite shaft strongly influences its dynamic behavior. Lim and Darlow [15] showed that, for optimally designing of composite drive shafts, the tube radius is determinable if the laminates, the shaft section length and operating speed are specified.

Using Sanders' best first approximation shell theory, Kim and Bert [16] analyzed a rotating shaft containing layers of arbitrarily laminated composite materials and determined its critical speeds. Both the thin- and thick-shell models, including the Coriolis effect, were presented. Lam and Loy [17] used Love's first approximation theory to study the vibration of thin rotating laminated cylindrical shells. They also illustrated the whirl speeds of a rotating composite shell by taking into account the Donnell's, Flügge's, Love's and Sanders' shell theories [18]. These results indicate that Donnell's theory holds well only for cylindrical shells with small L/R ratios (L is the length and R the radius of the shaft), and when the circumferential wave number is small. For shells with higher L/R ratios or when the circumferential wave number is non-negligible, the Love's theory is used for its higher accuracy and simplicity.

Bert [19] simplified the Bernoulli–Euler beam theory and provided analysis including bending–twisting coupling effects, to study the critical speeds of composite shafts. Bert and Kim [20] extended the above-mentioned analysis using the Bresse–Timoshenko beam model. Conventional beam model approaches used to date are equivalent modules beam theory (EMBT). Singh and Gupta [21] proposed a lateral, layerwise beam theory (LBT), which was derived from a layerwise shell theory, in the rotor dynamic analysis of a composite rotor. The results indicated that the critical speeds calculated by using LBT and EMBT methods correlate well. Singh and Gupta [22] also investigated the flexural vibration characteristics of composite cylindrical tubes, by considering only the first cicumferential modes, essentially the bending modes, and compared the results obtained from beam and shell theories. For the first two flexural frequencies, the results of the Timoshenko beam theory correlated well with those of the shell theory [22], for shells with L/R ratios ranging from 12–600. Therefore, for shell with high L/R ratios, Timoshenko beam theory predicts accurately the dynamic behavior of a composite cylindrical shell-type shaft.

The dynamic instability of a rotor-bearing system, subjected to periodic time dependent axial forces, is interesting. These forces may cause parametric vibration, a phenomenon that is characterized by unbounded growth of a small disturbance, eventually damaging the machine. Comprehensive studies of dynamic stability problems of machine components and structural members are summarized by Bolotin [23]. Chen and Ku [24] investigated the effect of rotatory inertia, transverse shear deformation and gyroscopic moment on the dynamic stability of a rotating shaft subjected to periodic axial compressive loads.

This paper describes a finite element model based upon the Timoshenko beam theory, to obtain matrix equations of motion for rotating shafts. The present analyses are validated by comparing both the flexural frequencies with a non-rotating cylindrical shell [8] and the critical speeds for the composite laminated shafts [13]. Critical whirl speeds are calculated by employing a whirl frame of reference. The dynamic stability of a rotating composite shaft subjected to a periodic axial compressive load is also illustrated. This study also delineates the effect of the rotation speeds and the disk on the unstable regions.

2. POTENTIAL AND KINETIC ENERGY

Figure 1 illustrates a uniform shaft with a disk subjected to an axial compressive load $P(t)$, and rotating at a constant speed Ω. The rotating frame (xyz) rotates about the X-axis through an angle Ωt with respect to the fixed frame (XYZ). This study presents the equations of motion for composite layered shell shafts and steel shafts (see Figure 2).

The equivalent modulus beam theory (EMBT) is used to study the dynamic behavior of the composite shaft. This approach provides accurate results for symmetric configurations and is easily extended to rotor dynamic analysis. However, the EMBT suffers from the following limitations: (i) it does not account for bending stretching coupling and shear normal coupling effects; (ii) it excludes the cross-sectional deformations and out of plane warping [21].

For an orthotropic layer, which the major material symmetry direction orients at an acute angle to the reference direction, the stress–strain relations are given as:

$$\begin{Bmatrix}\sigma_1\\ \sigma_2\\ \tau_6\end{Bmatrix} = \begin{bmatrix}\bar{Q}_{11} & \bar{Q}_{12} & \bar{Q}_{16}\\ \bar{Q}_{12} & \bar{Q}_{22} & \bar{Q}_{26}\\ \bar{Q}_{16} & \bar{Q}_{26} & \bar{Q}_{66}\end{bmatrix}\begin{Bmatrix}\varepsilon_1\\ \varepsilon_2\\ \gamma_6\end{Bmatrix}, \tag{1}$$

where σ_1 and σ_2 are in-plane normal stresses, τ_6 is the in-plane shear stress; ε_1 and ε_2 are in-plane normal strains, and γ_6 is the in-plane shear strain. The transformed $\bar{Q}$'s can be expressed in terms of the planar reduced stiffness Q's [25]. The following derivation

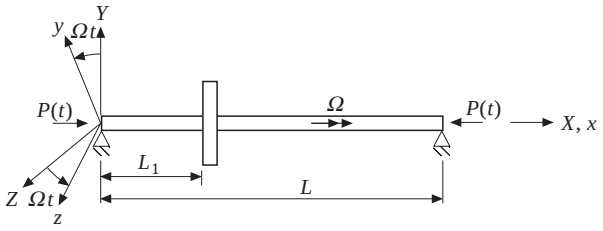

Figure 1. A rotating rotor–disk assembly subjected to axial compressive loads.

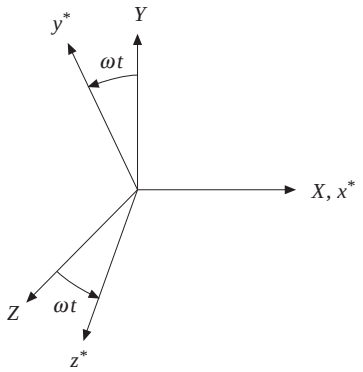

Figure 2. The whirl frame $(x^*y^*z^*)$ and the inertia frame (XYZ).

resembles that presented by Bert [19], where the bending and torsional energy for the laminate shaft are shown as:

$$U_1 = \sum_{k=1}^{N} \tfrac{1}{2} \int_V (\sigma_1^{(k)} \varepsilon_1^{(k)} + \tau_6^{(k)} \gamma_6^{(k)}) \, \mathrm{d}V, \tag{2}$$

Here N is the total number of layers, and

$$\varepsilon_1 = -y\beta' + z\alpha', \qquad \gamma_6 = \bar{r}\phi', \tag{3}$$

in which α, β and ϕ represent the rotations about the y-, z- and x-axes respectively; $\bar{r}$ is the radial component of the polar co-ordinate for the circular-cross-section shaft.

Using equations (1) and (3), the strain energy u_1 can be expressed as

$$U_1 = \tfrac{1}{2} \int_0^L [C_B(\alpha'^2 + \beta'^2) + C_T \phi'^2] \, \mathrm{d}x,$$

$$C_B = \frac{\pi}{4} \sum_{k=1}^{N} \bar{Q}_{11}^{(k)} [R_{o(k)}^4 - R_{i(k)}^4], \qquad C_T \equiv \frac{\pi}{2} \sum_{k=1}^{N} \bar{Q}_{66}^{(k)} [R_{o(k)}^4 - R_{i(k)}^4], \tag{4}$$

where C_B and C_T are the bending and torsional rigidities, and $R_{i(k)}$ and $R_{o(k)}$ are the inner and outer radii of the kth ply.

The out-of-plane shear strain energy is given by

$$U_2 = \tfrac{1}{2} \int_0^L C_S[(v' - \beta)^2 + (w' + \alpha)^2] \, \mathrm{d}x, \tag{5}$$

where the shear rigidity $C_S \equiv \bar{\kappa} G_{12} A$ and $\bar{\kappa} = 1/(2 - G_{12} v_{12}/E_1)$. (Dharmarajan and McCutchen [26]); G_{12} denotes the major shear modulus, v_{12}, the major Poisson's ratio, E_1, the major elasticity modulus. Adding equations (4) and (5), the total strain energy for the laminated composite shaft can be obtained as

$$U_{com} = U_1 + U_2 = \tfrac{1}{2} \int_0^L \{C_B(\alpha'^2 + \beta'^2) + C_T \phi'^2 + C_S[(v' - \beta)^2 + (w' + \alpha)^2]\} \, \mathrm{d}x. \tag{6}$$

The v and w represent the translations of the central line of the shaft in the y and z directions respectively. The prime ($'$) denotes differentiation with respect to the spatial co-ordinate x. This model assumes that the ply angle of the composite shaft is $(\pm\theta)_n$. This assumption results in the reduced stiffness $\bar{Q}_{16}$ being negligibly small, and therefore the bending–twisting coupling effect can be neglected.

Using the Timoshenko beam theory, the displacement fields of a shaft are described in the rotating frame (x, y, z) as

$$u_x(x, y, z, t) = -y\beta(x, t) + z\alpha(x, t), \, u_y(x, y, z, t) = v(x, t) - z\phi(x, t),$$

$$u_z(x, y, z, t) = w(x, t) + y\phi(x, t), \tag{7}$$

where u_x, u_y and u_z denote the displacement of the shaft in the x, y and z directions respectively. For an isotropic material, the strain– and stress–displacement relations of the shaft are

$$\varepsilon_{xx} = -y\beta' + z\alpha', \qquad \varepsilon_{xy} = \tfrac{1}{2}(-\beta + v' - z\phi'), \qquad \varepsilon_{xz} = \tfrac{1}{2}(\alpha + w' + y\phi') \tag{8}$$

and

$$\sigma_{xx} = E(-y\beta' + z\alpha'), \qquad \tau_{xy} = \kappa G(-\beta + v') - Gz\phi', \qquad \tau_{xz} = \kappa G(\alpha + w') + Gy\phi' \tag{9}$$

TABLE 1

Comparison of the present results with reported results for an orthotropic shell [8]. ($L = 0{\cdot}8$ m, $R = 0{\cdot}063$ m, $t = 0{\cdot}51$ mm, $E_{11} = 214$ GPa, $E_{22} = 18{\cdot}6$ GPa, $v_{12} = 0{\cdot}28$, $G_{12} = 5{\cdot}17$ GPa)

Investigator	Method	First bending (Hz)	Second bending (Hz)
Bert and Kumar [8]	TST	534	1290
	SDT1	533	1290
	SDT2	534	1290
Singh and Gupta [22]	TST	533·5	1289
	SDT1	533·4	1290
	TBT	533·3	1290
Present	TBT	534·5	1292·3

TST: thin shell theory; SDT1: shear deformable theory; SDT2: shear deformable theory with rotatory inertia; TBT: Timoshenko beam theory.

TABLE 2

Material properties and geometric parameters of the composite shaft

	Properties					
Material	E_1 (Gpa)	E_2 (Gpa)	v_{12}	$G_{12} = G_{13}$ (Gpa)	G_{23} (Gpa)	ρ
BE	211	24·1	0·36	6·90	6·90	1·967
GE	139	11·0	0·313	6·05	3·78	1·578

BE, Boron–epoxy, GE, Graphite–epoxy: geometric parameters length $L = 2{\cdot}47$ m; mean diameter = 12·69 cm; wall thickness = 1·321 mm.

TABLE 3

Critical speeds of the composite shaft with the layers of boron–epoxy and the stacking sequence $90^\circ/\pm 45^\circ/(0^\circ)_6/90^\circ$

Investigator	Method of determination	Critical speed (r.p.m.)
Zinberg and Symonds [13]	Theoretical	5780
	Experimental	5500
Bert [19]	Bernoulli–Euler beam theory	5919
Bert and Kim [20]	Bresse–Timoshenko beam theory	5788
Present	Timoshenko beam theory and finite element method	5714

The strain energy of the rotating shaft can be derived from equations (8) and (9).

$$U_{iso} = \tfrac{1}{2}\iiint_V (\sigma_{xx}\varepsilon_{xx} + 2\tau_{xy}\varepsilon_{xz} + 2\tau_{xz}\varepsilon_{xz})\,\mathrm{d}V$$

$$= \tfrac{1}{2}\int_0^L \{EI(\alpha'^2 + \beta'^2) + \kappa GA[(v' - \beta)^2 + (w' + \alpha)^2] + GI_P\phi'^2\}\,\mathrm{d}x, \tag{10}$$

where E is the Young's modulus, G the shear modulus, κ the shear correction factor, I the area moment of inertia and I_P the area polar moment of inertia.

The kinetic energy of the shaft, referred to the fixed frame (X, Y, Z), can be written as:

$$KE_s = \tfrac{1}{2}\int_0^L [\rho A(\dot{V}^2 + \dot{W}^2) + \rho I_P\dot{\phi}^2 + \rho I(\dot{\theta}_Y^2 + \dot{\theta}_Z^2) + 2\rho I_P\Omega\dot{\theta}_Y\theta_Z]\,\mathrm{d}x, \tag{11}$$

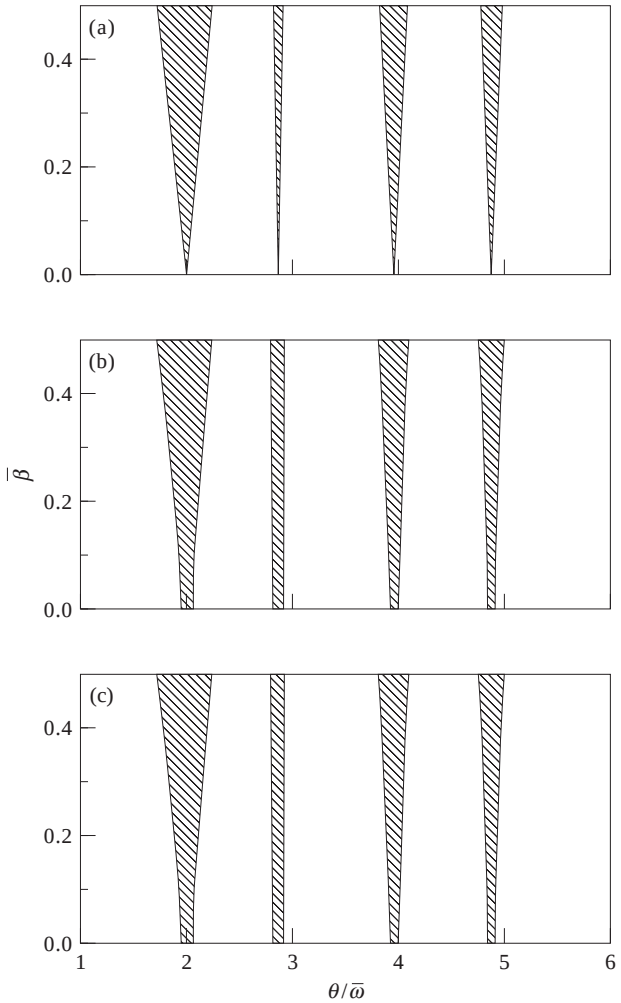

Figure 3. Regions of dynamic instability for the first mode of a rotating shaft, $P^* = 9{\cdot}717C_B/L^2$, $\varpi = 9{\cdot}778(C_B/\rho AL^4)^{1/2}$, $\bar{\alpha} = 0$. (a) $\Omega = 0$ r.p.m; (b) $\Omega = 10\,000$ r.p.m.; (c) $\Omega = 20\,000$ r.p.m. From left to right: $(\pm 60^\circ)_5$, steel, $(\pm 30^\circ)_5$, $(0^\circ)_{10}$.

where ρ is the density, V and W are the displacement along the Y- and Z-axes, θ_Y and θ_Z are the rotations about the Y- and Z-axes, and a dot $(\cdot)$ denotes differentiation with respect to time t. The kinetic energy form illustrated in equation (11) is used for isotropic and composite shafts.

Consider the disk as a rigid body, then the kinetic energy can be calculated by integrating equation (11) over the disk, with the deflection V, W, θ_Y and θ_Z assumed to be independent of x. The kinetic energy of the disk is expressed as

$$KE_d = \tfrac{1}{2}[M_d(\dot{V}_d^2 + \dot{W}_d^2) + J_P\dot{\phi}^2 + J(\dot{\theta}_{Yd}^2 + \dot{\theta}_{Zd}^2) + 2J_P\Omega\dot{\theta}_{Yd}\theta_{Zd}], \tag{12}$$

where M_d is the mass, J the mass moment of inertia and J_P the mass polar moment of inertia of the disk. Equations (11) and (12) consider the effects of rotatory inertia and gyroscopic moment.

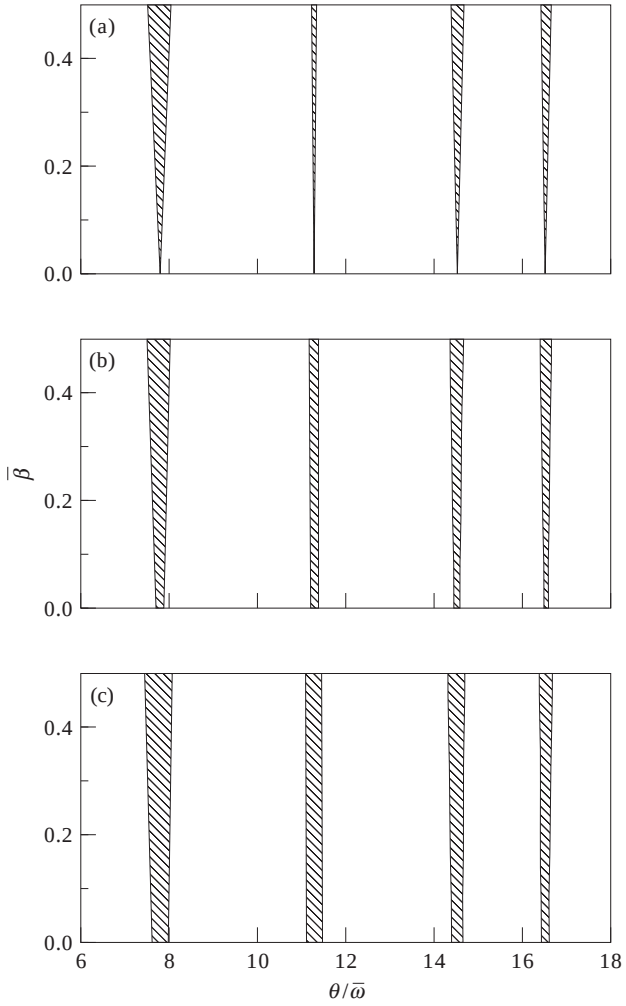

Figure 4. As Figure 3 but for the second mode.

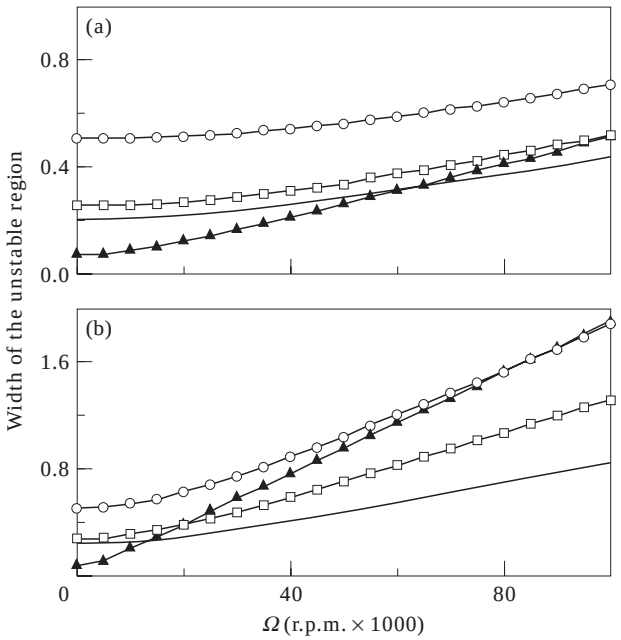

Figure 5. The width of the unstable region when $\bar{\alpha} = 0$ and $\overline{\beta} = 0{\cdot}5$. $P^* = 9{\cdot}717C_B/L^2$, $\varpi = 9{\cdot}778(C_B/\rho AL^4)^{1/2}$; (a) first mode, (b) second mode. Key: —, $(0^\circ)_{10}$; –□–, $(30^\circ)_5$; –○–, $(60^\circ)_5$; –▲–, steel.

A rotating shaft subjected to an axial compressive load $P(t)$ will perform work given by the following equation, which considers stability analysis.

$$W_p = \tfrac{1}{2}\int_0^L P(t)(v'^2 + w'^2)\,\mathrm{d}x. \tag{13}$$

In order to calculate the governing equations, the strain energy of a shaft should be expressed in the fixed frame. The displacement vector for the fixed frame is $\{\mathbf{Q}\} = \{V, W, \theta_Y, \theta_Z, \phi\}^{\mathrm{T}}$, and that for the rotating frame is $\{\mathbf{q}\} = \{v, w, \alpha, \beta, \phi\}^{\mathrm{T}}$. The two frames are related from $\{\mathbf{q}\} = [\mathbf{R}]\{\mathbf{Q}\}$, the transform matrix $[\mathbf{R}]$ is:

$$[\mathbf{R}] = \begin{bmatrix} \cos\Omega t & \sin\Omega t & 0 & 0 & 0 \\ -\sin\Omega t & \cos\Omega t & 0 & 0 & 0 \\ 0 & 0 & \cos\Omega t & \sin\Omega t & 0 \\ 0 & 0 & -\sin\Omega t & \cos\Omega t & 0 \\ 0 & 0 & 0 & 0 & 1 \end{bmatrix}. \tag{14}$$

The strain energy U_{com} and U_{iso} are defined as

$$U_{com} = \tfrac{1}{2}\int_0^L \{C_B(\theta_Y'^2 + \theta_Z'^2) + C_S[(V' - \theta_Z)^2 + (W' + \theta_Y)^2] + C_T\phi'^2\}\,\mathrm{d}x, \tag{15}$$

and

$$U_{iso} = \tfrac{1}{2}\int_0^L \{EI(\theta_Y'^2 + \theta_Z'^2) + \kappa GA[(V' - \theta_Z)^2 + (W' + \theta_Y)^2] + GI_P\phi'^2\}\,\mathrm{d}x, \tag{16}$$

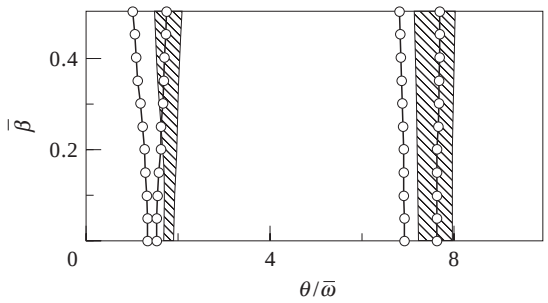

Figure 6. Effect of static load factor $\bar{\alpha}$ on the regions of dynamic instability of a rotating shaft, with the stacking sequence $(\pm 60^\circ)_5$, $\Omega = 40\,000$ r.p.m. Key: —, $\bar{\alpha} = 0{\cdot}2$; –○–, $\bar{\alpha} = 0{\cdot}5$.

The external work can be expressed as

$$W_p = \tfrac{1}{2} \int_0^L P(t)(V'^2 + W'^2)\, \mathrm{d}x. \tag{17}$$

3. THE FINITE ELEMENT EQUATION

The generalized co-ordinate at node **i**, i.e., two translations (V_i, W_i), three rotations (θ_{Yi}, θ_{Zi}, ϕ_i) and their derivatives (V_i', W_i', θ_{Yi}', θ_{Zi}', ϕ_i'), describe the finite element model.

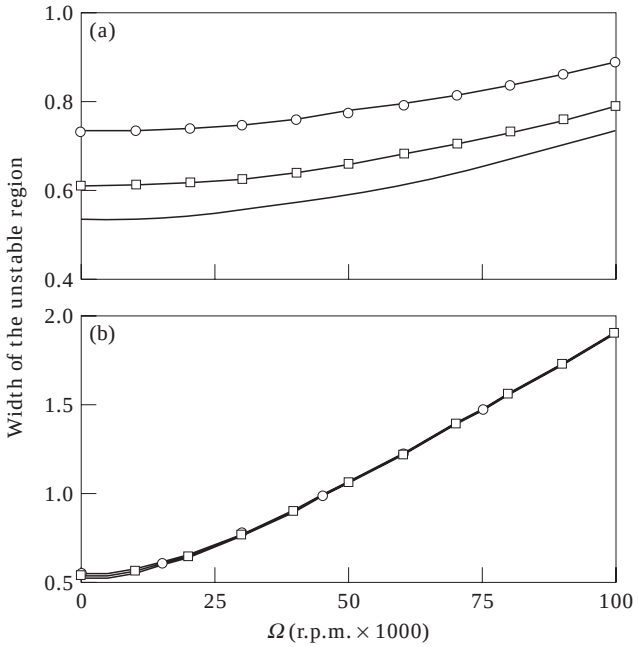

Figure 7. The width of the unstable region for the case of the stacking sequence $(\pm 60^\circ)_5$ at $\bar{\beta} = 0{\cdot}5$; (a) first mode, (b) second mode. Key: —, $\bar{\alpha} = 0{\cdot}1$; –□–, $\bar{\alpha} = 0{\cdot}3$; –○–, $\bar{\alpha} = 0{\cdot}5$.

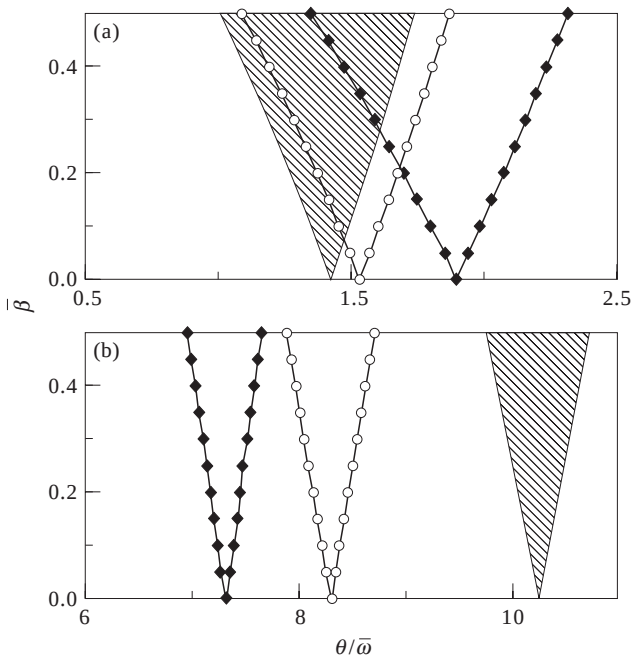

Figure 8. Regions of dynamic instability for the composite shaft with the stacking sequence $(90^\circ/\pm 45^\circ/(0^\circ)_6/90^\circ)$, $p^* = 9{\cdot}04C_B/L^2$, $\varpi = 6{\cdot}43(C_B/\rho AL^4)^{1/2}$, $\bar{\alpha} = 0{\cdot}5$, $\Omega = 0$ r.p.m.; (a) first mode, (b) second mode. Key: —, $L_1 = L/2$; –○–, $L_1 = L/3$; –◇–, $L_1 = L/6$.

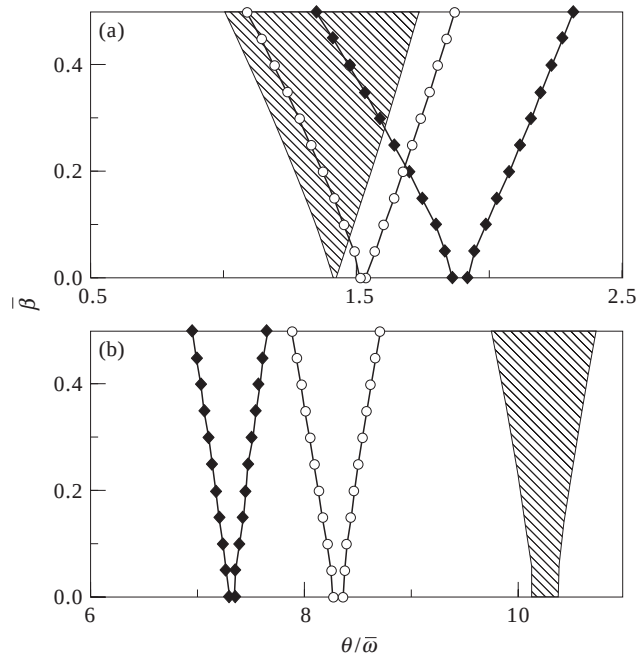

Figure 9. As Figure 8 but $\Omega = 10\,000$ r.p.m. Key as for Figure 8.

Then the displacement field of the element can be approximated as:

$$\begin{Bmatrix} V \\ W \\ \theta_Y \\ \theta_Z \\ \phi \end{Bmatrix} = \begin{bmatrix} V_i & V'_i & V_{i+1} & V'_{i+1} \\ W_i & W'_i & W_{i+1} & W'_{i+1} \\ \theta_{Yi} & \theta'_{Yi} & \theta_{Yi+1} & \theta'_{Yi+1} \\ \theta_{Zi} & \theta'_{Zi} & \theta_{Zi+1} & \theta'_{Zi+1} \\ \phi_i & \phi'_i & \phi_{i+1} & \phi'_{i+1} \end{bmatrix} \begin{Bmatrix} N_1(\xi) \\ N_2(\xi) \\ N_3(\xi) \\ N_4(\xi) \end{Bmatrix}, \tag{18}$$

where $N_i(\xi)$, $(i = 1, 2, 3, 4)$, represent the one dimensional local cubic Hermite polynomial shape function, where detailed forms are listed in Appendix A. If equation (18) is substituted into equations (11), (12) and (15–17), the potential energy U^e and the kinetic energy T^e can be rewritten in terms of the nodal displacement vector as

$$U^e = \tfrac{1}{2}\{\mathbf{Q}^e\}^{\mathrm{T}}[\mathbf{K}^e]\{\mathbf{Q}^e\} - \tfrac{1}{2}P(t)\{\mathbf{Q}^e\}^{\mathrm{T}}[\mathbf{K}_G^e]\{\mathbf{Q}^e\}, \tag{19}$$

$$T^e = \tfrac{1}{2}\{\mathbf{Q}^e\}^{\mathrm{T}}[\mathbf{M}^e]\{\mathbf{Q}^e\} - \tfrac{1}{2}\Omega\{\mathbf{Q}^e\}^{\mathrm{T}}[\mathbf{G}_Y^e]\{\mathbf{Q}^e\}, \tag{20}$$

Reformulating all elements, the Lagrangian functional L^* is expressed as

$$L^* = \sum_e (U^e - T^e). \tag{21}$$

Substituting equation (21) into Lagrange's equations gives

$$[\mathbf{M}]\{\ddot{\mathbf{Q}}\} - \Omega[\mathbf{G}_Y]\{\dot{\mathbf{Q}}\} + ([\mathbf{K}] - P(t)[\mathbf{K}_G])\{\mathbf{Q}\} = 0, \tag{22}$$

where $\{\mathbf{Q}\} = \{V_1, V'_1, W_1, W'_1, \ldots, \theta_{YN}, \theta'_{YN}, \theta_{Zn}, \theta'_{ZN}, \phi_N, \phi'_N\}^{\mathrm{T}}$ is the global nodal co-ordinates vector. $[\mathbf{M}]$ is the mass matrix, $[\mathbf{G}_Y]$, the gyroscopic matrix, $[\mathbf{K}]$, the stiffness matrix contribution of the strain energy of the shaft, and the geometric matrix $[\mathbf{K}_G]$, the axial load $P(t)$ contribution.

3.1. CRITICAL SPEED ANALYSIS

In order to validate the present model, critical speeds of the composite shaft are compared with those in previous works. The supports of the rotating shaft are assumed to be isotropic; therefore, a rotating reference frame can be used to analyze the whirl speeds of a rotating shaft under an axial load. The displacement variables between the fixed (XYZ) and the whirl $(x^*y^*z^*)$ frame co-ordinates are related as:

$$\{\mathbf{Q}\}^{\mathrm{T}} = [\mathbf{R}^*]\{\mathbf{p}\}^{\mathrm{T}}, \tag{23}$$

where

$$[\mathbf{R}^*] = \begin{bmatrix} \cos\omega t & -\sin\omega t & 0 & 0 & 0 \\ \sin\omega t & \cos\omega t & 0 & 0 & 0 \\ 0 & 0 & \cos\omega t & -\sin\omega t & 0 \\ 0 & 0 & \sin\omega t & \cos\omega t & 0 \\ 0 & 0 & 0 & 0 & 1 \end{bmatrix} \tag{24}$$

Since the displacement vector $\{\mathbf{p}\}$ is constant relative to the whirl frame $(x^*y^*z^*)$, the system's equations of motion can be simplified into the following form [27]

$$([\mathbf{K}] - P(t)[\mathbf{K}_G])\{\mathbf{p}\} - \omega^2([\mathbf{M}_T] + (1 - 2\lambda)[\mathbf{M}_R])\{\mathbf{p}\} = \{\mathbf{0}\}, \tag{25}$$

where $\lambda \equiv \Omega/\omega$ and ω is the whirl speed; $[\mathbf{M}] \equiv [\mathbf{M}_T] + [\mathbf{M}_R]$, $[\mathbf{M}_T]$ is the translational mass matrix and $[\mathbf{M}_R]$ is the rotatory inertia matrix. The whirl ratio λ is $+1$ for forward whirl mode and -1 for backward whirl mode.

3.2. DYNAMIC STABILITY ANALYSIS

A fraction of the non-rotating, fundamental static buckling load P^* can describe a rotating shaft subjected to a periodic axial force $P(t) = P_0 + P_t \cos \theta t$, where θ is the axial disturbance frequency, and the static and time dependent components of the load are given by

$$P(t) = \bar{\alpha} P^* + \bar{\beta} P^* \cos \theta t. \tag{26}$$

If the static and time dependent components of the load are applied similarly, then equation (22) changes to be following equation.

$$[\mathbf{M}]\{\ddot{\mathbf{Q}}\} - \Omega[\mathbf{G}_Y]\{\dot{\mathbf{Q}}\} + ([\mathbf{K}] - (\bar{\alpha} P^* + \bar{\beta} P^* \cos \theta t)[\mathbf{K}_G])\{\mathbf{Q}\} = 0. \tag{27}$$

Equation (27) represents a system of second order differential equations with periodic coefficients of the Mathieu–Hill type. The theory of linear equations with periodic coefficients predicts that the boundaries between stable and unstable regions can be constructed by periodic solutions of period T and $2T$, where $T = 2\pi/\theta$. The solutions with period $2T$ are important. Equation (28) describes a first approximation of the periodic solutions with period $2T$ [23]

$$\{\mathbf{Q}\} = \{\mathbf{a}\} \sin (\theta t/2) + \{\mathbf{b}\} \cos (\theta t/2). \tag{28}$$

Substituting equation (28) into equation (27) and equating the coefficients of the $\sin (\theta t/2)$ and $\cos (\theta t/2)$ terms provides a set of linear homogeneous algebraic equations in terms of $\{\mathbf{a}\}$ and $\{\mathbf{b}\}$. The conditions for the set of linear homogeneous equations to have non-trivial solutions is

$$\begin{vmatrix} [\mathbf{K}] - (\bar{\alpha} P^* - \bar{\beta} P^*/2)[\mathbf{K}_G] - (\theta^2/4)[\mathbf{M}] & (\Omega\theta/2)[\mathbf{G}_Y] \\ (\Omega\theta/2)[\mathbf{G}_Y] & [\mathbf{K}] - (\bar{\alpha} P^* + \bar{\beta} P^*/2)[\mathbf{K}_G] - (\theta^2/4)[\mathbf{M}] \end{vmatrix} = 0. \tag{29}$$

Equation (29) can be referred to as the equation of boundary frequencies, and can be used to calculate the boundaries of instability regions.

4. RESULTS AND DISCUSSION

Numerical results of the present method are compared with those in previous models. Table 1 lists the natural frequencies obtained by the present method and some reported frequencies. A comparison indicates that the configurations considering the equivalent modulus beam theory provide accurate values of the flexural frequencies. The critical speed of a thin-walled composite shaft with a ten-layered laminate was also examined, as investigated by Zinberg and Symonds [13]. The material properties and the geometric parameters are listed in Table 2. In Table 3, the critical speed of a boron–epoxy composite shaft is calculated by the present finite element beam model. The present model shows good agreement with those reported by other researchers.

The first two instability regions for a simply supported shaft are shaded in Figures 3 and 4. The rotational speeds Ω are included and the disk is excluded. A steel shaft of the same geometric parameters as those of a graphite-epoxy composite shaft, shown in Table 2, is considered in the study. The material properties of the steel shaft are $E = 207\text{E}9$ Pa, $G = 79{\cdot}6\text{E}9$ Pa, $\kappa = 0{\cdot}53$, $\rho = 7680$ kg/m^3. P^* and ϖ, as shown in Figures 3 and 4, are the

non-rotating fundamental static buckling load and natural frequency of the composite shaft with a stacking sequence of $(\pm 60^\circ)_5$. When $\bar{\alpha} = 0$ and $\overline{\beta} = 0$, the solution of equation (29) provides the natural frequencies ($\omega = \theta/2$). Figure 3(a) shows that the natural frequency ratio (θ/ϖ) are twice the roots of the shaded regions for non-rotating shafts. The fundamental frequency of the steel shaft is smaller than when the ply orientation is $(\pm 30^\circ)_5$ and $(0^\circ)_{10}$, but larger than when the ply orientation is $(\pm 60^\circ)_5$. The unstable region of the steel shaft is much smaller than that of the composite one. The second mode also shows similar results obtained for the first mode (see Figure 4(a)). This phenomenon is due to the composite shaft being more sensitive to the axial compressive load. The unstable regions, for the same mode, when the stacking sequence is $(\pm 60^\circ)_5$, are larger than those of $(\pm 30^\circ)_5$ and $(0^\circ)_{10}$. Therefore, increasing the fiber angles θ shifts the unstable region closer to the dynamic load factor axis and broadens the region, if the stacking sequence of the composite shaft is represented as $(\pm\theta)_n$. The stacking sequence of the composite layers has exerted a significant effect on the dynamic stability characteristic of a rotating composite shaft. When the rotational speed increases, the boundaries of the regions of dynamic stability shift away from each other and unstable regions broaden (Figures 3 and 4), since the gyroscopic moment is proportional to the rotational speed. It can be concluded that the gyroscopic moment destabilizes the dynamic stability for the composite and steel shafts. Chen and Ku [24] arrived at a similar conclusion.

The effect of rotational speed on the width of the unstable regions is illustrated in Figure 5. It is evident that as the rotational speed increases, the width of the second mode region enlarges more rapidly than for the first mode. In addition, the unstable region of the steel case is increased faster than the other composite cases. Thus, the gyroscopic moment exerts a larger destabilizing effect on the steel shaft than on the composite shaft can be seen in these diagrams. The influence of this gyroscopic moment is different because the steel shaft is denser than the composite one.

Figure 6 illustrates the effects of the static load factor $\bar{\alpha}$ on the unstable regions. As the static load factor increases, the unstable regions shift to the left and the width of the first region increases; thus the rotating shaft is more unstable. Figure 7 describes the effects of the rotational speed and the static load component on the unstable region. It shows that, with different $\bar{\alpha}$, the width of the unstable region is different for the first mode, but is quite closed for the second mode.

Figures 8 and 9 show the influence of the position of the disk on the composite shaft. The geometric parameters of the disk are $M_d = 1{\cdot}5\,\text{kg}$, $J = 0{\cdot}004\,\text{kgm}^2$ and $J_P = 0{\cdot}008\,\text{kgm}^2$. When the disk is shifted nearer to the supported end ($x = 0$), the first unstable regions in Figures 8(a) and 9(a) shift to the right (higher frequency ratio) and the widths of these regions increase; however, when the distance L_1 decreases, the unstable regions of the second mode shift to the left and the widths of these regions decrease. Therefore, for a lower disturbance frequency of the axial load, the rotating shaft with a disk at the center ($L_1 = L/2$) is more stable than the other cases, but is less stable than the other two cases when a higher disturbance frequency is applied.

5. CONCLUSIONS

The Timoshenko beam and a finite element technique was used to model the laminated composite shaft and to determine the regions of dynamic instability of the rotating shaft. The present numerical results agree with those in reported literature. The natural frequency of the composite shaft would be higher than the steel shaft for the same geometric parameters. Owing to its higher density, the steel shaft is more sensitive to the rotational speed than is the composite shaft. The stacking sequence of the composite shaft profoundly

effects the critical speed and the dynamic stability of the composite shaft. The influence of the disk on the dynamic stability is also studied in this work. Decreasing the length L_1 causes broadening of the first unstable region, and narrowing of the second region. Therefore, a decrease in the length L_1 makes the rotating shaft less stable when a lower disturbance frequency is applied and more stable when a higher disturbance frequency is applied.

ACKNOWLEDGMENT

The authors sincerely acknowledge the financial assistance of the National Science Council under Grant No. NSC 84-2212-E-006-088.

REFERENCES

1. S. B. Dong 1968 *The Journal of the Acoustical Society of America* **44**, 1628–1635. Free vibration of laminated orthotropic cylindrical shells.
2. C. W. Bert, J. L. Baker and D. M. Egle 1969 *Journal of Composite Materials* **3**, 480–499. Free vibrations of multilayer anisotropic cylindrical shells.
3. J. Padovan 1975 *Computers & Structures* **5**, 145–154. Numerical analysis of asymmetric frequency and buckling eigenvalues of prestressed rotating anisotropic shells of revolution.
4. R. C. Fortier and J. N. Rossettos 1973 *Journal of Applied Mechanics* **40**, 299–301. On the vibration of shear deformable curved anisotropic composite plates.
5. S. B. Dong and F. K. W. Tso 1972 *Journal of Applied Mechanics* **39**, 1091–1097. On a laminated orthotropic shell theory including transverse shear deformation.
6. B. K. Rath and Y. C. Das 1973 *Journal of Sound and Vibration* **28**, 737–757. Vibration of layered shells.
7. Y. S. Hsu, J. N. Reddy and C. W. Bert 1981 *Journal of Thermal Stresses* **4**, 155–177. Thermoelasticity of circular cylindrical shells laminated of bimodulus composite materials.
8. C. W. Bert and M. Kumar 1982 *Journal of Sound and Vibration* **81**, 107–121. Vibration of cylindrical shells of bimodulus composite materials.
9. C. H. J. Fox and D. J. W. Hardie 1985 *Journal of Sound and Vibration* **101**, 495–510. Harmonic response of rotating cylindrical shells.
10. A. Smirnov 1989 *Journal of Applied Mechanics* **56**, 423–429. Free vibrations of the rotating shells of revolution.
11. Y. Chen, H. B. Zhao, Z. P. Shen, I. Grieger and B.-H. Kröplin 1993 *Journal of Sound and Vibration* **160**, 137–160. Vibrations of high speed rotating shells with calculations for cylindrical shells.
12. K. R. Sivadas and N. Ganesan 1994 *Journal of Vibration and Acoustics* **116**, 198–202. Effect of rotation on vibration on moderately thick circular cylindrical shells.
13. H. Zinberg and M. F. Symonds 1970 *26th Annual Forum of the American Helicopter Society*, 1–14. The development of advanced composite tail rotor driveshaft.
14. H. L. M. dos Reis, R. B. Goldman and P. H. Verstrate 1987 *Journal of Composites Technology and Research* **9**, 58–62. Thin-walled laminated composite cylindrical tubes: part III—critical speed analysis.
15. J. W. Lim and M. S. Darlow 1986 *Journal of American Helicopter Society*, 75–83. Optimal sizing of composite power transmission shafting.
16. C. D. Kim and C. W. Bert 1993 *Composites Engineering* **3**, 633–643. Critical speed analysis of laminated composite, hollow shafts.
17. K. Y. Lam and C. T. Loy 1994 *Composites Engineering* **4**, 1153–1167. On vibrations of thin rotating laminated composite cylindrical shells.
18. K. Y. Lam and C. T. Loy 1995 *Journal of Sound and Vibration* **186**, 23–35. Analysis of rotating laminated cylindrical shells by different thin shell theories.
19. C. W. Bert 1993 *Proceeding of the 6th Japan-U.S. Conference on Composite Materials*, 29–36. The effect of bending–twisting coupling on the critical speed of a driveshaft.
20. C. W. Bert and C.-D. Kim 1995 *Journal of Vibration and Acoustics* **117**, 17–21. Whirling of composite-material driveshafts including bending–twisting coupling and transverse shear deformation.

21. S. P. Singh and K. Gupta 1996 *Journal of Sound and Vibration* **191**, 739–756. Composite shaft rotordynamic analysis using a layerwise theory.
22. S. P. Singh and K. Gupta 1994 *Journal of Sound and Vibration* **172**, 171–190. Free damped flexural vibration analysis of composite cylindrical tubes using beam and shell theories.
23. V. V. Bolotin 1964 *The Dynamic Stability of Elastic Systems*. San Francisco: Holden-Day.
24. L.-W. Chen and D.-M. Ku 1990 *Journal of Sound and Vibration* **143**, 143–151. Dynamic stability analysis of a rotating shaft by the finite element method.
25. R. M. Jones 1975 *Mechanics of Composite Materials*. New York: McGraw-Hill.
26. S. Dharmarajan and H. McCutchen Jr 1973 *Journal of Composite Materials* **7**, 530–535. Shear coefficients for orthotropic beams.
27. D.-M. Ku and L.-W. Chen 1994 *Modal analysis*: *the International Journal of Analytical and Experimental Modal Analysis* **9**, 111–123. Stability and whirl speeds of rotating shaft under axial loads.

APPENDIX

The cubic Hermite polynomial shape functions:

$$N_1(\xi) = (2 - 3\xi + \xi^3)/4, \qquad N_2(\xi) = (1 - \xi - \xi^2 + \xi^3)/4,$$

$$N_3(\xi) = (2 + 3\xi - \xi^3)/4, \qquad N_4(\xi) = (-1 - \xi - \xi^2 + \xi^3)/4.$$

The element matrices:

$$[\mathbf{M}_T] = \begin{bmatrix} (A_{ij}) & 0 & 0 & 0 & 0 \\ 0 & (A_{ij}) & 0 & 0 & 0 \\ 0 & 0 & 0 & 0 & 0 \\ 0 & 0 & 0 & 0 & 0 \\ 0 & 0 & 0 & 0 & (C_{ij}) \end{bmatrix}_{20\times 20}, \qquad [\mathbf{M}_R] = \begin{bmatrix} 0 & 0 & 0 & 0 & 0 \\ 0 & 0 & 0 & 0 & 0 \\ 0 & 0 & (B_{ij}) & 0 & 0 \\ 0 & 0 & 0 & (B_{ij}) & 0 \\ 0 & 0 & 0 & 0 & 0 \end{bmatrix}_{20\times 20},$$

$$[\mathbf{G}_Y] = \begin{bmatrix} 0 & 0 & 0 & 0 & 0 \\ 0 & 0 & 0 & 0 & 0 \\ 0 & 0 & 0 & -2(B_{ij}) & 0 \\ 0 & 0 & 2(B_{ij}) & 0 & 0 \\ 0 & 0 & 0 & 0 & 0 \end{bmatrix}_{20\times 20},$$

$$[\mathbf{K}] = \begin{bmatrix} (D_{ij}) & 0 & 0 & (H_{ij}) & 0 \\ 0 & (D_{ij}) & (F_{ij}) & 0 & 0 \\ 0 & (G_{ij}) & (E_{ij}) & 0 & 0 \\ (I_{ij}) & 0 & 0 & (E_{ij}) & 0 \\ 0 & 0 & 0 & 0 & (J_{ij}) \end{bmatrix}_{20\times 20},$$

$$[\mathbf{K}_G] = \begin{bmatrix} (L_{ij}) & 0 & 0 & 0 & 0 \\ 0 & (L_{ij}) & 0 & 0 & 0 \\ 0 & 0 & 0 & 0 & 0 \\ 0 & 0 & 0 & 0 & 0 \\ 0 & 0 & 0 & 0 & 0 \end{bmatrix}_{20\times 20},$$

where,

$$(A_{ij}) = \int \rho A N_i N_j \, \mathrm{d}x, \qquad (B_{ij}) = \int \rho I N_i N_j \, \mathrm{d}x, \qquad (C_{ij}) = \int \rho I_P N_i N_j \, \mathrm{d}x,$$

$$(D_{ij}) = \int C_S N_i' N_j' \, \mathrm{d}x, \qquad (E_{ij}) = \int [C_B N_i' N_j' + C_S N_i N_j] \, \mathrm{d}x,$$

$$(F_{ij}) = \int C_S N_i' N_j \, \mathrm{d}x, \qquad (G_{ij}) = \int C_S N_i N_j' \, \mathrm{d}x, \qquad (H_{ij}) = \int -C_S N_i' N_j \, \mathrm{d}x,$$

$$(I_{ij}) = \int -C_S N_i N_j' \, \mathrm{d}x,$$

$$(J_{ij}) = \int C_T N_i' N_j' \, \mathrm{d}x, \qquad (L_{ij}) = \int N_i' N_j' \, \mathrm{d}x, \qquad i, j = 1, 2, 3, 4.$$

The above equations are for a composite shaft; if an isotropic shaft is used, the coefficients C_B, C_S and C_T will be replaced by EI, κGA, and GI_P respectively.